Surrogate-based Global Sensitivity Analysis of Seat-belt Design Parameters on Thoracic Injury in Far-Side Impacts Using a Human Body Model

Junik Cho, Changmin Baek, Yun Seok Kang, Dongjin Lee

Abstract Far-side impacts pose a substantial thoracic injury risk, yet rib-level responses to varying load and occupant factors remain insufficiently characterised. We developed a human body model (HBM) parametric framework to investigate the influence of seat-belt geometry, impact severity, and occupant posture on rib strain under far-side loading. After generating simulation data via a mixed-factor design of experiments (DOE), we performed a variance-based global sensitivity analysis (GSA) to quantify rib-specific main and interaction effects. For computational efficiency, we used a collaborative multi-output Gaussian process (CoMOGP) surrogate to model correlated rib responses, while fitting a polynomial dimensional decomposition (PDD) surrogate separately for GSA. We also mapped the peak maximum principal strain (MPS) in each rib to fracture risk. The results showed that impact severity governed overall strain levels across most ribs, while occupant posture and seat-belt geometry influenced localised rib-specific redistribution, particularly in the lower ribs. Injury-risk mapping further showed that selected lower ribs retained variable fracture-risk responses across the severity–posture combinations and seat-belt geometry variations. CoMOGP reduced average prediction error relative to a baseline single-output GP, although improvements varied across ribs. This method can guide future restraint system optimisation by prioritising key design variables and injury-relevant ribs across various seating postures.

Keywords Far-side impact, Global sensitivity analysis, Multi-output surrogate model, Rib strain, Seat-belt geometry.

I. INTRODUCTION

The thorax is a critical body region at risk of serious injury in far-side crashes, with loading arising from occupant excursion, restraint interaction, and contact with interior structures during far-side motion [1]. Post-mortem human subjects (PMHS) test series have further shown that rib fractures are common under far-side sled loading conditions representative of real-world crash severities [2-3]. Euro NCAP is transitioning to virtual testing protocols that use human body models (HBMs), with strain-based rib fracture assessments planned for implementation from 2029 onwards [4]. This shift increases the need for systematic rib-strain analysis, as rib strain serves as a primary indicator of cortical bone failure in simulated impacts.

Previous far-side studies have advanced our understanding of far-side thoracic loading but have largely characterised the response through occupant-level kinematics and restraint interaction rather than rib-level strain. Earlier work [5] showed, through a validated MADYMO human model, that D-ring position and pretension influenced shoulder-belt slip-off and altered the belt-to-thorax load path. A subsequent 36-test PMHS series [6] varied D-ring position, arm position, pelvis restraint, pretensioning, and impact severity in lateral and oblique conditions, revealing the sensitivity of thoracic restraint interaction to multiple factors and providing kinematic corridors for HBM validation. A follow-up study [7] benchmarked WorldSID responses against these PMHS corridors and identified discrepancies in belt engagement and torso kinematics, underscoring the need for HBM-based evaluation of rib-level injury metrics inaccessible to physical surrogates. More recently, a far-side assessment method based on response surfaces used HBM simulations and neural network metamodels to predict occupant-level outcomes, including maximum lateral head excursion and thoracic AIS3+ injury probability, as functions of occupant anthropometry, impact direction, and restraint configuration [8]. These previous studies demonstrated that belt geometry, pretension, impact direction, and occupant variability govern far-side occupant

D. Lee (e-mail: dlee46@hanyang.ac.kr) is an Assistant Professor, J. Cho is an MSc student and C. Baek is a PhD student in the Department of Automotive Engineering at Hanyang University, Seoul, South Korea. Y. S. Kang is an Associate Professor and Director of the Injury Biomechanics Research Lab at The Ohio State University, USA.

response, but they primarily focused on occupant-level kinematics or injury outcomes rather than rib-wise strain responses. To the authors' knowledge, no study has used a HBM to systematically quantify how seat-belt geometry, impact severity, and occupant posture jointly affect rib-wise strain responses or how their main and interaction effects vary across individual ribs. We expect such interaction effects to be important because belt routing, crash pulse magnitude, and occupant position simultaneously govern the occupant's excursion path, and thus the sequence and location of rib loading.

A global sensitivity analysis (GSA) framework addresses this gap by decomposing the total output variance into main and interaction effects across the full input space, without assumptions of linearity or monotonicity [9-10]. In far-side loading, individual ribs are loaded through distinct contact and restraint paths during occupant excursion, so the sensitivity pattern is expected to vary across rib levels. Moreover, rib strain may respond non-monotonically to posture and restraint geometry, as postural changes can shift the primary load path between rib groups rather than uniformly scaling strain across the thorax [11]. Therefore, resolving rib-specific main and interaction effects is necessary to identify which factor combinations dominate strain variability at each rib level.

Rib strain responses across the thorax are inherently interdependent. While ribs experience shared inertial and restraint loading during far-side motion, their individual strain levels vary due to rib geometry (e.g. local curvature), cross-sectional properties (e.g. cortical thickness), and boundary conditions at the sternum (e.g. costochondral joints) and thoracic vertebrae (e.g. costovertebral joints) [12]. Despite this coupling, rib strain or fracture probability has been evaluated independently before aggregation to the rib-cage level [13]. Given limited HBM simulation budgets, this isolated approach discards inter-rib correlations that could regularise predictions in sparsely sampled regions. Consequently, adopting a multi-output modelling framework that leverages these dependencies is expected to improve estimation accuracy over traditional single-output models [14].

This study uses GSA to examine the main and interaction effects of seat-belt geometry, impact severity, and occupant posture on rib strain responses under far-side loading. We focus on two main objectives: (1) identifying the factors that dominate rib-specific strain variability; and (2) determining the predictive advantages of collaborative multi-output surrogate modelling. Together, these objectives provide a basis for interpreting far-side thoracic response at the individual rib level rather than only at the rib-cage level.

II. METHODS

Our study followed a clear sequential workflow. We first validated the baseline HBM sled configuration against PMHS reference corridors. We then ran HBM simulations using a space-filling maximum projection (MaxPro) design of experiments (DOE) [15]. Next, we applied a collaborative multi-output Gaussian process (CoMOGP) model to leverage the correlated behaviour among ribs [16]. Separately, we fitted a polynomial dimensional decomposition (PDD) surrogate directly to the HBM simulation responses to quantify the main and interaction effects via variance-based GSA [17-18].

HBM-based Computational Modelling in a Far-side Configuration

We adopted a finite element (FE) sled model from the Euro NCAP HBM4VT validation catalogue to represent the far-side sled environment in [2]. We used version 1.0.0 of this set-up, including the assessment notebook. The model consists of an oblique buck configuration with the vehicle X-axis oriented at 75° relative to the sled longitudinal axis. This sled model includes a rigid seat, centre console, and foot/leg side plate; the console and side plate are represented as rigid bodies covered with 50 mm Ethafoam.

The occupant was represented using the Global Human Body Models Consortium (GHBMC) 50th percentile male simplified HBM, M50-OS v2.3.2. The H-point was defined following the PMHS test configuration [2]. Figure 1 shows that the restraint system consisted of a 3-point seat-belt with a retractor, and the baseline belt hard-point locations were subsequently varied according to the design parameters examined in this study.

Before crash loading, a 400 ms settling phase was applied to stabilise the HBM and achieve belt fit. During this phase, pelvis and thorax constraints were imposed and gravity was disabled. The occupant was settled by accelerating the seat upward at 1 g while simultaneously restoring the footrest and console to their initial positions with a 200 N belt pretension. Figure 2 shows the resulting initial occupant position and belt fit.

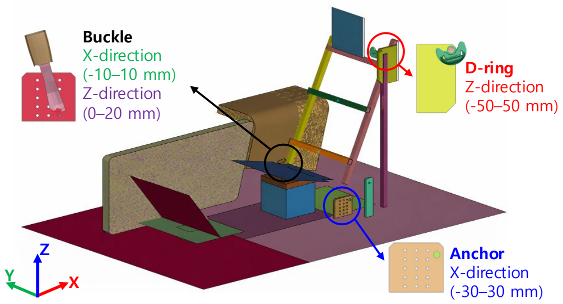

Fig. 1. Baseline computational far-side sled model and seat-belt geometry variables.

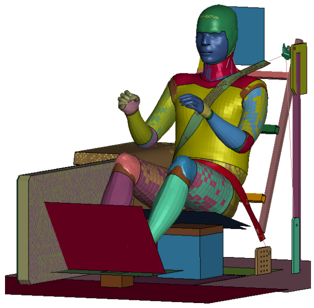

Fig. 2. Initial position of the HBM in the far-side sled model after the settling phase.

After the settling phase, the pelvis and thorax constraints were released, gravity was activated, and the oblique sled loading was applied through the prescribed X- and Y-direction velocity components. Figure 3 shows the buck orientation relative to the sled. Figure 4 shows the reference validation pulse corresponding to ΔV = 8 m/s. No pretensioner or load limiter was included in the crash phase because the study focused on the restraint response without active devices. All simulations were performed using LS-DYNA R12.2.1 (MPP single precision) on a Linux server with AMD EPYC 9554 processors.

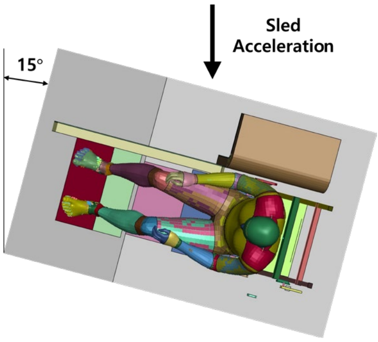

Fig. 3. Orientation of the buck relative to the sled.

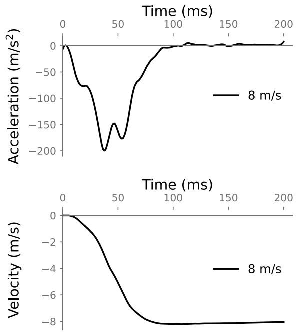

Fig. 4. Sled deceleration and velocity pulses.

Baseline Model Validation

To assess the suitability of the baseline HBM configuration for the subsequent parametric analysis, we validated the model against reference PMHS test data under matched loading and boundary conditions. The validation was performed at ΔV = 8 m/s using the baseline HBM configuration described above, including the buck orientation, initial occupant positioning, restraint set-up, and prescribed sled pulse. The comparison channels included head Y- and Z-displacements, shoulder-belt force, lap-belt force, console Y force, and seat Z force. Because PMHS responses exhibit substantial inter-subject variability, an ARCGen-based statistical corridor method was adopted to represent the characteristic response trend and experimental variability of the PMHS data [19]. Head Y- and Z-displacements were quantitatively scored using Ellipse and DALW metrics to quantify agreement with PMHS corridors, consistent with the Euro NCAP evaluation framework. Force-channel comparisons provided supplementary evidence of restraint and contact loading reproduction. The baseline model satisfied the minimum validation criteria specified in the Euro NCAP qualification and comparability procedures [4].

Input Variables

To represent realistic variation in seat-belt hard-point geometry across vehicle platforms, the Z-axis positions of the D-ring and buckle and the X-axis positions of the buckle and lap-belt anchor were varied. Table I summarises these parameters as displacements from the baseline restraint configuration. Hard-point variations were implemented as translations from the baseline coordinates. For the D-ring Z-position, we translated the D-ring slip-ring rigid part and the associated shoulder anchor part together in the Z-direction. For the buckle variables, we translated the buckle and buckle strap in the prescribed X- or Z-direction. For the lap-belt anchor variable, we translated the belt anchor in the X-direction. When translating each hard-point assembly, we updated the associated belt nodes defining the 1D belt path consistently with the new hard-point location, thereby re-establishing the belt routing for the modified configuration. The seat, console, and side-plate geometries were unchanged. Appendix B shows these configurations. We considered three impact severities (ΔV = 8 m/s, 11 m/s, and 14 m/s). We generated the 11 m/s and 14 m/s levels by scaling the 8 m/s reference pulse using calibrated scale factors to achieve the target ΔV values while preserving the original pulse shape and duration. Appendix C shows the resulting pulse profiles. Three occupant postures were considered: erect (baseline), moderate slouched, and extreme slouched. The moderate and extreme slouched postures were defined using previously reported forward pelvis displacements of 40 and 60 mm, respectively [20], consistent with previous studies [21-22].

TABLE I
INPUT VARIABLES

Variable	Type	Levels or range	Units
D-ring Z position (X_1)	Continuous	-50–50	mm
Anchor X position (X_2)	Continuous	-30–30	mm
Buckle Z position (X_3)	Continuous	0–20	mm
Buckle X position (X_4)	Continuous	-10–10	mm
Impact severity (X_5)	Categorical	8, 11, 14	m/s
Occupant posture (X_6)	Categorical	Erect, Moderate slouched, Extreme slouched	–

We implemented different postures in Oasys PRIMER using the marionette method. During positioning, PRIMER generated the standard cable system for the HBM skeleton. Following the procedure in [20], we modified only the target positions of the cables associated with the pelvic bones to generate the slouched postures, leaving the thoracic and lumbar spine, arms, legs, and feet without active repositioning. We applied no additional segment-level constraints or translational/rotational degree-of-freedom locks in any direction during posture generation. Consequently, positional changes in the other body regions resulted passively from the pelvis positioning process. For the moderate and extreme slouched conditions, the pelvic target positions were adjusted to achieve the prescribed forward pelvis displacements of 40 mm and 60 mm, respectively, relative to the erect posture, shifting the ASIS and H-point forward accordingly. Figure 5 shows the resulting postures.

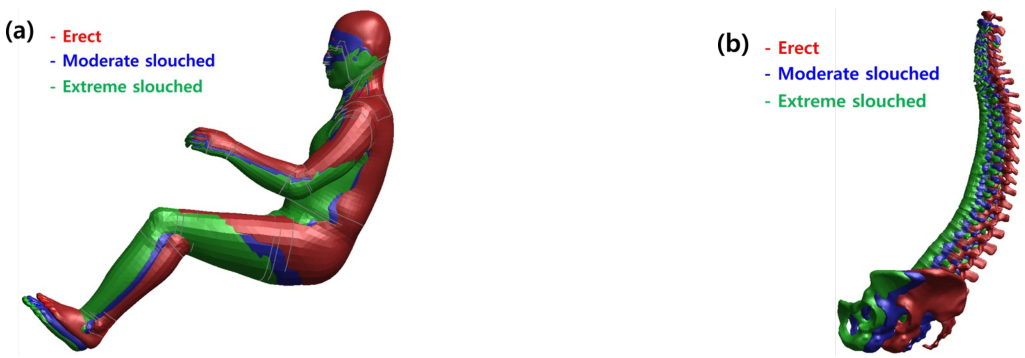

Fig. 5. Overlaid HBMs for three posture conditions: (a) whole-body lateral view; (b) pelvis–spine lateral view. The erect, moderate slouched, and extreme slouched postures are shown in red, blue, and green, respectively.

Figure 5(b) shows that relative to the erect posture (red), the pelvis angle increased by 3.22° in the moderate slouched posture (blue) and by 7.31° in the extreme slouched posture (green). The corresponding ASIS X-position shifts were 42.18 mm forward for the moderate slouched posture and 60.64 mm forward for the extreme slouched posture. These changes were broadly consistent with previously reported posture trends [20].

Design of Experiments (DOE)

We used the mixed-factor MaxPro framework [15] to explore the design space efficiently. As shown in Table I, the design space comprised four continuous seat-belt geometry variables and two categorical factors: impact severity and occupant posture. The MaxPro framework preserves balanced coverage of both the full design space and the design space of each severity–posture subspace used in the subsequent response and sensitivity analyses.

Based on the two categorical factors, nine slices of the design space were defined from all combinations of the three impact severities and three posture levels. A total of 180 simulation cases were generated, with 20 design points assigned to each slice. Impact severity was treated as a categorical factor for DOE construction, ensuring balanced representation of all severity–posture combinations. The severity–posture combinations were fixed a priori to define the slice structure, and optimisation was performed only for the continuous seat-belt geometry variables within this structure. These factor treatments were chosen to match the role of each analysis stage.

The mixed-factor MaxPro criterion used as the general design formulation is given by [15]:

$$\psi(\boldsymbol{D}) = \left\{ \frac{1}{\binom{n}{2}} \sum_{i=1}^{n-1} \sum_{j=i+1}^{n} \frac{1}{\prod_{l=1}^{p_1} \left(x_{il} - x_{jl}\right)^2 \prod_{k=1}^{p_2} \left\{ \left|u_{ik} - u_{jk}\right| + \frac{1}{m_k} \right\}^2 \prod_{h=1}^{p_3} \left\{ I\left(v_{ih} \neq v_{jh}\right) + \frac{1}{L_h} \right\}^2} \right\}^{\frac{1}{p_1+p_2+p_3}} \quad (1)$$

where all symbols are defined in Appendix A.

Design generation proceeded within the predefined slice structure based on all combinations of impact severity and occupant posture. Within these slices, an initial Latin hypercube design (LHD) [23] was generated for the continuous variables and then refined by simulated annealing (SA) [24] to minimise the MaxPro criterion and improve space-filling properties. In this optimisation step, the severity–posture slice was kept fixed, and only the continuous seat-belt geometry coordinates were adjusted to improve within-slice and overall space-filling. The resulting 180 cases were used as the training dataset for the surrogate modelling described below.

Multi-output Surrogate Modelling

We adopted Gaussian process (GP) regression as the surrogate modelling framework. GP regression can represent non-linear relationships between inputs and responses while also providing predictive uncertainty [25]. However, modelling each rib response independently with single-output models does not exploit the dependency structure among the rib responses. To account for these inter-rib dependencies, a CoMOGP model was adopted [16]. This formulation was attractive in the present setting because all ribs were loaded within the same far-side event, and the outputs were expected to contain both event-level shared structure and rib-specific deviations.

In the CoMOGP framework, the response of the d-th output at input $\mathbf{x}$ is written as:

$$y_d(\mathbf{x}) = \sum_{q=1}^{Q} a_{d,q} g_q(\mathbf{x}) + h_d(\mathbf{x}) + \epsilon_d \quad (2)$$

where all symbols are defined in Appendix A. In this study, $D = 24$ (corresponding to the 24 rib responses) and $Q = 3$. The shared and output-specific latent functions were assigned zero-mean GP priors. In biomechanical terms, the shared latent functions can be interpreted as capturing common response patterns associated with global occupant motion, whereas the output-specific terms capture rib-specific deviations. Impact severity was treated as an ordered physical variable in the GP kernel, whereas posture was represented categorically because similarity between posture levels could not be assumed to vary monotonically.

To enable sparse collaboration across outputs, inducing variables were introduced for the shared and output-specific latent functions. For each shared latent function $g_q(\mathbf{x})$, a set of shared inducing variables was defined as:

$$\mathbf{u}_q = g_q\left(\mathbf{Z}_{\mathrm{q}}\right) \quad (3)$$

where the symbols are defined in Appendix A. For each output-specific latent function, a set of individual inducing variables was defined as:

$$\mathbf{v}_d = h_d\left(\mathbf{Z}_{\mathrm{d}}^h\right) \quad (4)$$

where the symbols are defined in Appendix A. The shared inducing variables provide the mechanism for information transfer across outputs, whereas the individual inducing variables preserve output-specific flexibility.

The CoMOGP model training procedure is summarised as follows. Step 1 (Sparse representation): for each shared latent function, define shared inducing variables via Eq. (3); for each output-specific latent function, define individual inducing variables via Eq. (4). The numbers of shared and output-specific inducing points were set to

$M_g = 60$ and $M_h = 30$, respectively. Step 2 (Variational inference): approximate the posterior using the sparse variational formulation in Eq. (5):

$$q(\mathbf{g}, \mathbf{h}, \mathbf{u}, \mathbf{v} \mid \mathbf{y}) = p(\mathbf{g} \mid \mathbf{u}) p(\mathbf{h} \mid \mathbf{v}) q(\mathbf{u}, \mathbf{v}) \tag{5}$$

where all symbols are defined in Appendix A. Step 3 (Covariance specification): define the product covariance kernel for the shared and output-specific latent functions via Eq. (6):

$$k\left((\mathbf{x}_i, c_i), (\mathbf{x}_j, c_j)\right) = k_{SE}(\mathbf{x}_i, \mathbf{x}_j) k_{cat}(c_i, c_j) \tag{6}$$

where the symbols are defined in Appendix A. The kernel k_{SE} is a squared-exponential kernel with automatic relevance determination (SE-ARD) for the four seat-belt geometry variables and impact severity, and k_{cat} is a categorical kernel for posture. The same covariance form was used for both latent-function types. Step 4 (Parameter estimation): jointly learn the mixing coefficients, kernel hyperparameters, inducing locations, and variational posterior parameters by maximising the evidence lower bound (ELBO), decomposed across inputs and outputs. Step 5 (Prediction): predict each rib response at a new input using the trained CoMOGP posterior mean and variance. The model was trained on 180 DOE cases and evaluated against the single-output baseline using an independent validation set. We quantified prediction error using standardised mean squared error (SMSE), which normalises mean squared error by validation-response variance. Lower SMSE indicates better prediction; zero denotes perfect prediction, whereas a value near one indicates performance no better than predicting the validation-set mean. We also reported the coefficient of determination (R^2) as a complementary metric.

PDD-based Global Sensitivity Analysis

The response metric for the sensitivity and surrogate analyses was the rib-wise 95th percentile maximum principal strain (MPS) of cortical bone, representing near-peak rib strain while reducing sensitivity to isolated extreme values. In this study, GSA was used to evaluate the relative importance of the input variables over the design space while accounting for both non-linearity and interaction effects. Because direct variance-based analysis using HBM simulations would be computationally impractical, we fitted a PDD surrogate directly to the HBM responses and obtained sensitivity indices from the fitted representation, avoiding thousands of additional direct simulations. Variance-based sensitivity analysis partitions the total response variance into contributions from individual inputs and their interactions, and PDD provides an efficient surrogate representation for this purpose [17-18]. This was particularly suitable here because the objective was not only response approximation but also direct variance decomposition into rib-specific main and interaction contributions.

As an orthonormal polynomial expansion based on analysis of variance (ANOVA), PDD represents the response using polynomial component functions of increasing interaction order [17]. In practice, a truncated PDD approximation was used because the full PDD expansion contains an infinite number of polynomial terms and associated coefficients [17]. In this study, a bivariate third-order approximation was adopted, with $N = 6$, $m = 3$, and $S = 2$. This truncation retained pairwise interaction effects while keeping the number of basis terms manageable relative to the available training data. The associated truncated PDD expression is given as:

$$Y \approx f_{S,m}(\mathbf{X}) := f_0 + \sum_{i=1}^{N} \sum_{j=1}^{m} \alpha_{ij} \psi_{ij}(X_i) + \sum_{i_1=1}^{N-1} \sum_{i_2=i_1+1}^{N} \sum_{j_1=1}^{m} \sum_{j_2=1}^{m} \beta_{i_1 i_2 j_1 j_2} \psi_{i_1 j_1}(X_{i_1}) \psi_{i_2 j_2}(X_{i_2}) \tag{7}$$

where all symbols are defined in Appendix A. For the PDD approximation, impact severity was treated as an ordered numeric input, whereas posture was represented through level-based numerical encoding for inclusion in the polynomial basis expansion.

For the sensitivity analysis, all input variables were assumed to follow uniform distributions over their prescribed levels or ranges. Accordingly, Legendre polynomials were used as the orthogonal basis functions in the PDD representation. The expansion coefficients were estimated using a regression-based procedure. Because correlations among basis terms could lead to unstable coefficient estimates, ridge regression was adopted for robust coefficient estimation. This regularised regression step was used to stabilise the coefficient estimates of the truncated expansion rather than to change the underlying variance-based interpretation of the PDD model.

Once the expansion coefficients had been estimated, the sensitivity indices were obtained directly from the fitted PDD representation. Owing to the orthonormality of the polynomial basis, the total variance and the partial variances associated with the univariate and bivariate terms were obtained directly from the squared PDD coefficients [17-18]. The first-order and second-order sensitivity indices were then defined as:

$$S_i = \frac{V_i}{\mathrm{Var}[Y]} \tag{8}$$

$$S_{i_1,i_2} = \frac{V_{i_1,i_2}}{\mathrm{Var}[Y]} \tag{9}$$

where all symbols are defined in Appendix A.

The PDD approximation retained only bivariate interactions; therefore, the total-effect sensitivity index of X_i was approximated by summing its first-order contribution and all associated second-order contributions, i.e.:

$$T_i \approx S_i + \sum_{k \neq i} S_{ik} \tag{10}$$

where T_i is the total-effect sensitivity index defined in Appendix A [17]. Based on Eqs. (8–10), first-order, second-order, and total-effect sensitivity indices were evaluated for each rib response to identify the dominant variables and pairwise interactions governing rib-level strain variability. This approach enabled the sensitivity structure of each rib response to be quantified at a manageable computational cost and provided a consistent basis for comparing patterns of main and interaction effects across the rib set.

III. RESULTS

Baseline Validation Results

Table II summarises the baseline validation scores for head kinematics, with the head Y- and Z-displacement responses yielding Ellipse/DALW scores of 0.72/0.89 and 0.69/0.94, respectively, both meeting the corresponding Euro NCAP HBM qualification criteria against the PMHS reference data in [2]. Overall, the simulation reproduced the main excursion characteristics of the PMHS corridors (Figure E2, Appendix E). Appendix D provides a visual comparison of the PMHS and HBM baseline configurations and gross kinematics, while supplementary qualitative comparisons of the shoulder-belt, lap-belt, console Y, and seat Z forces are provided in Figure E1 (Appendix E).

TABLE II
QUANTITATIVE VALIDATION SCORES FOR HEAD DISPLACEMENT RESPONSES

	Min. Ellipse Score	HBM Ellipse Score	Min. DALW Score	HBM DALW Score
Head Y Displacement	0.22	0.72	0.88	0.89
Head Z Displacement	–	0.69	0.56	0.94

Quality of the MaxPro DOE

The optimised MaxPro design provided superior space-filling: simulated annealing reduced the MaxPro criterion by 15.2% relative to the initial LHD. In the full design space, the four-dimensional minimum inter-point distance was 36.73% and 46.72% higher than random LHD and Marginally Coupled Design (MCD) [26], respectively, and remained 53.25% and 84.89% higher in categorical slices (Appendix F).

Rib Strain Patterns Across Severity and Posture

We evaluated rib responses for the cortical bone part sets of the left and right ribs. The rib-wise response metric was defined as the 95th percentile of element-level MPS. This robust, near-peak measure reduces the influence of isolated high-strain values associated with element quality issues, local contact effects, or artificial stress concentrations, while remaining straightforward to apply consistently across ribs and models [27-28]. Figure 6 summarises the baseline rib strain responses for the nine baseline conditions defined by the three impact severities and three posture levels, with the seat-belt geometry fixed at the baseline configuration.

Rib strain increased with ΔV across all posture conditions, with the strongest amplification in the right lower ribs (right ribs 10–12: 1.6–2.4 × between lowest and highest severities across postures). At fixed ΔV, posture-related changes were rib-dependent and often non-monotonic. The right lower ribs (especially right ribs 10–12) showed a clearer decrease–increase trend across posture levels that became more apparent at 14 m/s, whereas the left ribs exhibited more variable, rib-specific behaviour.

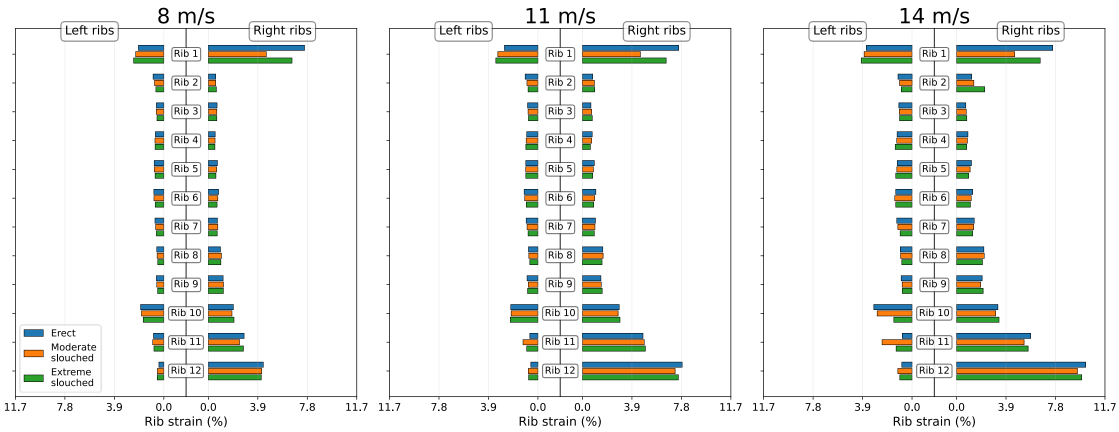

Fig. 6. Rib-wise baseline strain responses under the baseline seat-belt geometry at three impact severities (8 m/s, 11 m/s, and 14 m/s). Each panel displays the left and right rib strains separately, with bars representing the rib-wise 95th percentile MPS for each of the three posture conditions.

To provide injury-risk context for the rib strain responses, we mapped the peak MPS in each rib to rib-level fracture risk using the age-adjusted rib cortical bone fracture risk function from [29]. We performed this analysis separately from the surrogate modelling and GSA, which used the rib-wise 95th percentile MPS as the robust response metric. We set the occupant age to 45 years following the approach in [30] to approximate the average strain sensitivity across the age span of the bone samples used to construct the risk function.

Figure 7 summarises rib-wise fracture-risk distributions across the full DOE. Several ribs showed near-saturated risk (right ribs 1, 11, 12 and left rib 1 all had median risks ≥99.8% and >77% of cases exceeding 95%). In contrast, selected lower ribs showed clearer severity-related transitions. For right rib 8, the median risk increased from 3.0–4.5% at 8 m/s to 88.4–90.5% at 14 m/s across posture conditions; right ribs 9 and 10 showed similar severity-driven increases.

Selected lower ribs (left ribs 10 and 11) exhibited wide interquartile ranges (up to 72.9 percentage points) in slouched postures at higher severities, indicating strong geometry-induced variability. These findings guided the subsequent sensitivity interpretation toward lower ribs with non-saturated and variable fracture-risk responses.

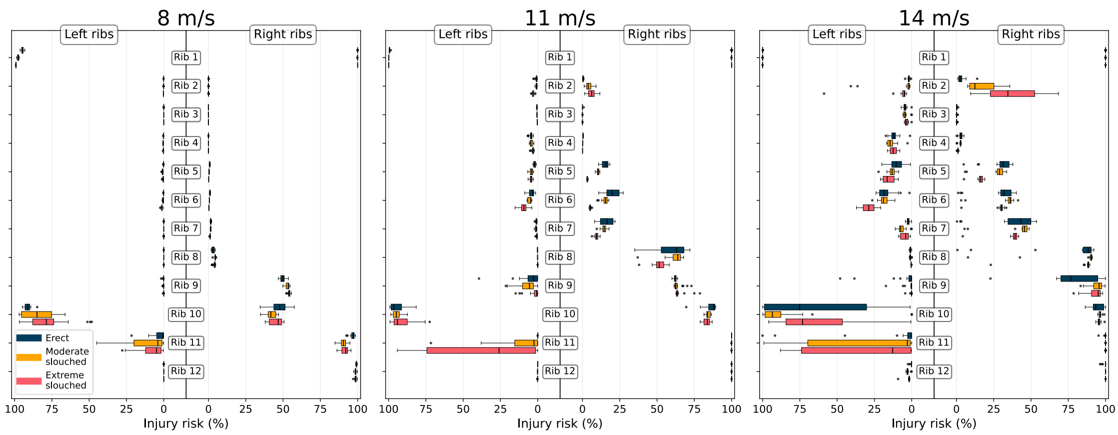

Fig. 7. Rib-wise fracture-risk distributions across the full DOE at impact severities of 8 m/s, 11 m/s, and 14 m/s. For each severity–posture condition, each box represents the 20 seat-belt geometry cases; boxes indicate the 25th–75th percentile range, centre lines indicate the median, whiskers indicate the non-outlying range based on the 1.5×IQR criterion, and grey dots indicate individual cases beyond the whiskers.

PDD-based Global Sensitivity Analysis Results

We performed PDD-based GSA on the rib-wise 95th percentile MPS responses of all left and right ribs over the full design space. Figure 8 presents representative results for selected ribs with non-saturated and variable fracture-risk responses, as identified in Figure 7. These ribs illustrate the dominant and contrasting sensitivity patterns across the rib set. Appendix G provides the full rib-wise results for all left and right ribs.

For the selected right lower ribs, impact severity remained the dominant contributor to the variance in the rib strain response. In right rib 8, impact severity accounted for 66.9% of the variance, followed by lap-belt anchor X-position with a contribution of 14.9%. Right rib 10 showed a similar severity-dominated pattern, although the contribution of impact severity was lower at 49.2%, while lap-belt anchor X-position made a larger secondary contribution of 27.2%. These patterns match the severity-related fracture-risk transition observed in Figure 7 for the right lower ribs, while also indicating a secondary influence from the lap-belt anchor position.

In contrast, the selected left lower ribs showed more distributed sensitivity patterns involving posture, belt geometry, and interaction effects. In left rib 10, posture was the largest contributor, accounting for 20.3% of the variance, followed by the interaction between D-ring Z-position and impact severity at 18.4%. Lap-belt anchor X-position and the interaction between impact severity and posture also contributed 11.6% and 8.5%, respectively. Lap-belt anchor X-position influenced left rib 11 most strongly, accounting for 38.5% of the variance, followed by the interaction between lap-belt anchor X-position and posture at 13.7% and posture alone at 10.6%.

Overall, the selected ribs showed two distinct sensitivity patterns. Impact severity primarily governed right ribs 8 and 10, consistent with their severity-related fracture-risk increase, whereas posture, belt geometry, and interaction terms yielded greater contributions for left ribs 10 and 11. Thus, the representative ribs with non-saturated and variable fracture-risk responses showed contrasting strain-sensitivity patterns across the selected lower-rib regions.

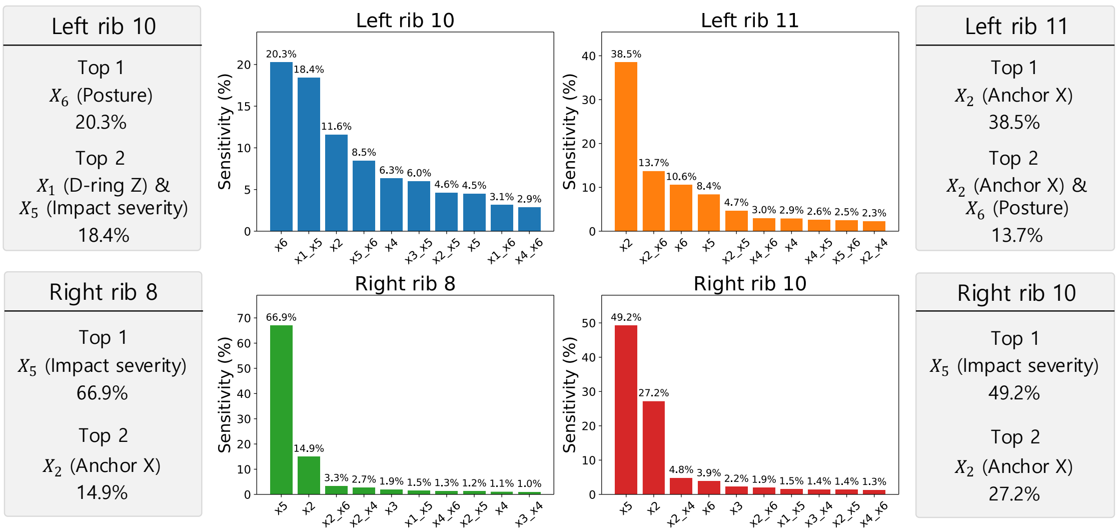

Fig. 8. Representative PDD-based GSA results for selected left and right rib strains. Bars show the relative contributions of the dominant variables and interactions to the variance of each response. X_1: D-ring Z-position; X_2: lap-belt anchor X-position; X_3: buckle Z-position; X_4: buckle X-position; X_5: impact severity; X_6: occupant posture. Terms of the form X_i denote main effects, whereas terms of the form $X_i\_X_j$ denote pairwise interaction effects.

Comparison of CoMOGP and SOGP Predictive Performance

We evaluated CoMOGP predictive performance on an independent 27-case validation set, comprising three cases per severity–posture combination. Prediction accuracy was compared against the SOGP baseline, in which each rib response was modelled separately. CoMOGP achieved an 8.43% reduction in average SMSE relative to SOGP across the rib set, with the largest gains observed in left rib 1 (71.09%) and right rib 12 (59.62%). However, the improvement was not uniform across ribs, and CoMOGP showed higher SMSE than SOGP for selected ribs, including left ribs 11 and 12. The full rib-wise comparison metrics and the per-rib percentage improvements in SMSE and R^2 are provided in Appendix H (Figure H1 and Table HI).

IV. DISCUSSION

The results show that rib-level thoracic response under far-side loading is not mechanically uniform across the rib cage. Impact severity governed the overall level of the 95th percentile MPS, whereas occupant posture and selected seat-belt geometry variables influenced the redistribution of strain across individual ribs. Under the baseline seat-belt geometry, the stronger posture-related variation observed at 14 m/s suggests that posture effects became more evident as impact severity increased. Within this design space, far-side thoracic loading therefore reflects a combination of a global severity-driven component and rib-specific redistribution.

The clearest heterogeneity was observed in the lower-rib region. Anatomically, the true ribs 1–7 appeared to follow the global severity-driven trend more consistently, whereas the false ribs 8–12 showed greater variability and clearer side-to-side asymmetry. Within the false ribs, the floating ribs 11 and 12 require separate consideration because they lack anterior sternal attachment and contributed to the most distinctive lower-rib response pattern observed in this study. The contrasting sensitivity patterns among the selected lower ribs may therefore reflect both anatomical and kinematic differences. The severity-dominated responses of the selected right lower ribs may be associated with increased torso excursion and restraint- or console-related contact loading at higher ΔV. In contrast, the left lower ribs showed larger contributions from posture, lap-belt anchor position, D-ring position, and their interactions, suggesting that load-path redistribution governs the response more than simple scaling with impact severity. In far-side motion, changes in belt routing can alter pelvis restraint, upper-torso rotation, and the timing and direction of lower-thorax loading. These kinematic changes may particularly influence ribs 10 and 11 because they are located in the lower thorax, and rib 11 lacks the anterior attachment present in the upper ribs. Therefore, the sensitivity of left ribs 10 and 11 to belt geometry and posture suggests that their responses were associated with lower-thorax load-path changes rather than global impact severity alone. Although this interpretation remains qualitative, it is consistent with previous far-side studies linking thoracic response to occupant kinematics, restraint condition, and lower-rib interaction with the console region [2][6].

The surrogate-modelling results further support joint modelling of the rib responses. CoMOGP yielded lower average prediction error than the single-output baseline, consistent with shared statistical structure across ribs, although the benefit was not uniform and does not by itself establish a specific mechanical coupling mechanism. At the same time, the mixed predictive performance in the left lower-rib region, particularly the higher SMSE of CoMOGP than SOGP in left ribs 11 and 12, indicates that shared cross-rib information was not equally beneficial for all outputs in this region. Together with the more distributed sensitivity patterns observed in the selected left lower ribs, this result suggests that the left lower-rib region exhibited more localised and variable response behaviour under this loading condition.

These findings indicate that rib-cage-level severity trends alone are insufficient for restraint assessment and design. The injury-risk results reinforce this point by showing that ribs with high fracture risk do not necessarily provide identical design insights. Near-saturated ribs identify regions associated with consistently high predicted fracture risk within the analysed DOE, whereas ribs with variable, non-saturated fracture-risk responses are more informative for distinguishing the injury-relevant effects of restraint-design changes. In practical restraint-system development, this rib-level sensitivity information can be used as an early screening basis to prioritise variables associated with posture-dependent lower-rib responses for further design refinement. Specifically, future restraint optimisation should consider not only reductions in global thoracic loading but also whether belt-routing changes redistribute loads toward vulnerable lower ribs in slouched postures. Additionally, the multi-output surrogate modelling of correlated rib responses can support future studies evaluating multiple rib-level objectives under limited HBM simulation budgets. This method helps define a refined set of design variables, rib-level objectives, and posture conditions for subsequent restraint optimisation.

This study has several limitations. Although additional kinematic landmarks, such as T1 and T8, are often examined in HBM validation studies, only the head Y- and Z-displacements are formally scored for this far-side loading condition in the Euro NCAP qualification framework. Accordingly, the validation emphasis was placed on the scored head responses, while the force responses were used as supplementary evidence of restraint and contact loading reproduction. We used a simplified far-side sled environment rather than a full vehicle model. The seat was modelled as rigid, and the centre console and side plate as rigid foam-covered structures. The restraint system excluded a pretensioner, load limiter, and airbag during the crash phase. The analysis was limited to a single HBM configuration, one oblique far-side loading condition, and a finite set of posture and seat-belt hard-point variations. In addition, the sensitivity analysis and injury-risk mapping were based on different rib strain summaries. The surrogate modelling and GSA used the rib-wise 95th percentile MPS as a robust response metric, whereas the fracture-risk mapping relied on the peak MPS in each rib. Readers should therefore interpret the GSA results as strain-response sensitivities supplemented by an injury-risk context, rather than as direct sensitivity indices of fracture risk itself. Accordingly, the findings should be interpreted as mechanistic trends within a controlled loading environment rather than direct predictions for all production-vehicle far-side crashes.

Future work should extend this framework to more representative far-side crash conditions, including a full vehicle interior, deformable seats, and production restraint systems with airbags, pretensioners, and load limiters. Expanding the design space to include additional occupant and restraint factors would also be valuable, as would improving surrogate robustness in the lower-rib region, where the behaviour remained localised and variable.

V. CONCLUSION

This study applied a surrogate-based GSA to characterise the influence of seat-belt geometry, impact severity, and occupant posture on rib-level strain during far-side impacts. While impact severity governed the overall strain across the rib cage, occupant posture and specific seat-belt geometry variables influenced rib-specific strain redistribution. The lower-rib region exhibited the greatest heterogeneity and sensitivity to local configuration changes, distinguishing it from the more uniform upper and mid ribs. The injury-risk analysis further showed that selected lower ribs yielded more informative insights for evaluating injury-relevant effects of impact severity, posture, and restraint geometry, as they retained variable, non-saturated fracture-risk responses across conditions. By decomposing these rib-specific responses into main and interaction effects, the PDD-based GSA provides an efficient screening approach for prioritising injury-relevant rib regions and key design variables in future posture-robust restraint optimisation. In parallel, the CoMOGP improved average predictive performance over single-output modelling by leveraging inter-rib correlation, though this improvement varied across individual ribs. These findings demonstrate that far-side thoracic response cannot be fully characterised by a rib-cage-level severity trend alone and needs to be assessed at the individual rib level. Future work should extend this framework to full-vehicle environments with production restraint systems while considering a broader range of occupant and restraint conditions.

VI. ACKNOWLEDGEMENTS

This work was partially supported by Hyundai Motor Company through the project "Development of an Injury Risk Analysis Method Considering Body-Type Uncertainty Using the GHBMC Model."

VII. REFERENCES

[1] Bostrom, O., Gabler, H. C., Digges, K., Fildes, B., Sunnevang, C. (2008) Injury Reduction Opportunities of Far side Impact Countermeasures. *Annals of Advances in Automotive Medicine*, **52**: pp. 289–300.

[2] Petit, P., Trosseille, X., *et al.* (2019) Far Side Impact Injury Threshold Recommendations Based on 6 Paired WorldSID / Post Mortem Human Subjects Tests. *Stapp Car Crash Journal*, **63**: pp. 127–146.

[3] Pintar, F. A., Yoganandan, N., *et al.* (2007) Comparison of PMHS, WorldSID, and THOR-NT Responses in Simulated Far Side Impact. *Stapp Car Crash Journal*, **51**: pp. 313–360.

[4] Euro NCAP (2025) *Crash Protection Technical Bulletin CP 550: Qualification Procedure for Human Body Models*. Euro NCAP, Leuven, Belgium.

[5] Douglas, C. A., Fildes, B. N., Gibson, T. J., Boström, O., Pintar, F. A. (2007) Factors Influencing Occupant-To-Seat Belt Interaction in Far-Side Crashes. *Annual Proceedings of the Association for the Advancement of Automotive Medicine*, **51**: pp. 319–339.

[6] Forman, J. L., Lopez-Valdes, F., *et al.* (2013) Occupant Kinematics and Shoulder Belt Retention in Far-Side Lateral and Oblique Collisions: A Parametric Study. *Stapp Car Crash Journal*, **57**: pp. 343–385.

[7] Perez-Rapela, D., Markusic, C., *et al*. (2018) Comparison of WorldSID to PMHS kinematics in far-side impact. *Proceedings of the IRCOBI Conference*, 2018, Athens, Greece, pp. 630–654.

[8] Perez-Rapela, D., Forman, J. L., Huddleston, S. H., Crandall, J. R. (2021) Methodology for vehicle safety development and assessment accounting for occupant response variability to human and non-human factors. *Computer Methods in Biomechanics and Biomedical Engineering*, **24**(4): pp. 384–399.

[9] Sobol, I. M. (2001) Global sensitivity indices for nonlinear mathematical models and their Monte Carlo

estimates. *Mathematics and Computers in Simulation*, **55**: pp. 271–280.

[10] Saltelli, A., Annoni, P., *et al*. (2010) Variance based sensitivity analysis of model output. Design and estimator for the total sensitivity index. *Computer Physics Communications*, **181**: pp. 259–270.

[11] Kang, Y. S., Stammen, J., *et al*. (2023) Thoracic responses and injuries to male postmortem human subjects (PMHS) in rear-facing seat configurations in high-speed frontal impacts. *Traffic Injury Prevention*, **24**(sup1): pp. 47–54.

[12] Agnew, A. M., Murach, M. M., *et al.* (2018) Sources of Variability in Structural Bending Response of Pediatric and Adult Human Ribs in Dynamic Frontal Impacts. *Stapp Car Crash Journal*, **62**: pp. 119–192.

[13] Forman, J. L., Kent, R. W., *et al*. (2012) Predicting Rib Fracture Risk With Whole-Body Finite Element Models: Development and Preliminary Evaluation of a Probabilistic Analytical Framework. *Annals of Advances in Automotive Medicine*, **56**: pp. 109–124.

[14] Liu, H., Cai, J., Ong, Y.-S. (2018) Remarks on Multi-Output Gaussian Process Regression. *Knowledge-Based Systems*, **144**: pp. 102–121.

[15] Joseph, V. R., Gul, E., Ba, S. (2020) Designing computer experiments with multiple types of factors: The MaxPro approach. *Journal of Quality Technology*, **52**(4): pp. 343–354.

[16] Nguyen, T. V., Bonilla, E. V. (2014) Collaborative Multi-output Gaussian Processes. *Proceedings of the Thirtieth Conference on Uncertainty in Artificial Intelligence*, 2014, Quebec City, Quebec, Canada, pp. 643–652.

[17] Rahman, S. (2018) Mathematical Properties of Polynomial Dimensional Decomposition. *SIAM/ASA Journal on Uncertainty Quantification*, **6**(2): pp. 816–844.

[18] Lee, D., Lavichant, E., Kramer, B. (2024) Global sensitivity analysis with limited data via sparsity-promoting D-MORPH regression: Application to char combustion. *Journal of Computational Physics*, **511**: p. 113116.

[19] Hartlen, D. C., Cronin, D. S. (2022) Arc-Length Re-Parametrization and Signal Registration to Determine a Characteristic Average and Statistical Response Corridors of Biomechanical Data. *Frontiers in Bioengineering and Biotechnology*, **10**: p. 843148.

[20] Bohman, K., Fågelberg, E., Jakobsson, L. (2023) Investigating slouching in frontal impacts using an HBM in the rear seat. *Proceedings of the 27th International Technical Conference on the Enhanced Safety of Vehicles*, 2023, Yokohama, Japan. Paper No. 23-0300.

[21] Beck, B., Brown, J., Bilston, L. E. (2014) Assessment of Vehicle and Restraint Design Changes for Mitigating Rear Seat Occupant Injuries. *Traffic Injury Prevention*, **15**(7): pp. 711–719.

[22] Uriot, J., Potier, P., *et al.* (2015) Comparison of HII, HIII and THOR dummy responses with respect to PMHS sled tests. *Proceedings of the IRCOBI Conference*, 2015, Lyon, France.

[23] McKay, M. D., Beckman, R. J., Conover, W. J. (1979) A Comparison of Three Methods for Selecting Values of Input Variables in the Analysis of Output from a Computer Code. *Technometrics*, **21**(2): pp. 239–245.

[24] Morris, M. D., Mitchell, T. J. (1995) Exploratory designs for computational experiments. *Journal of Statistical Planning and Inference*, **43**(3): pp. 381–402.

[25] Rasmussen, C. E., Williams, C. K. I. (2006) *Gaussian Processes for Machine Learning*, p. 272. *The MIT Press*: Cambridge, Massachusetts.

[26] Deng, X., Hung, Y., Lin, C. D. (2015) Design for computer experiments with qualitative and quantitative factors. *Statistica Sinica*, **25**(4): pp. 1567–1581.

[27] Forman, J., Kulkarni, S., Perez-Rapela, D., Mukherjee, S., Panzer, M., Hallman, J. (2022) A Method for Thoracic Injury Risk Function Development for Human Body Models. *Proceedings of the IRCOBI Conference*, 2022, Porto, Portugal, pp. 719–733.

[28] Takahira, Y., Katsumata, S., Yamamoto, T., Masuda, M. (2023) Probability Functional Evaluation of Chest Injury Based on Rib Strain of Human Body Model in Frontal Collision. *Proceedings of the 27th International Technical Conference on the Enhanced Safety of Vehicles*, 2023, Yokohama, Japan. Paper No. 23-0218.

[29] Larsson, K.-J., Blennow, A., Iraeus, J., Pipkorn, B., Lubbe, N. (2021) Rib Cortical Bone Fracture Risk as a Function of Age and Rib Strain: Updated Injury Prediction Using Finite Element Human Body Models. *Frontiers in Bioengineering and Biotechnology*, **9**: p. 677768.

[30] Larsson, K.-J., Iraeus, J., Holcombe, S., Pipkorn, B. (2023) Influences of Human Thorax Variability on Population Rib Fracture Risk Prediction Using Human Body Models. *Frontiers in Bioengineering and Biotechnology*, **11**: p. 1154272.

VIII. APPENDIX

Appendix A: Nomenclature

Symbols used in the equations and statistical formulations throughout this paper are summarised below. Equation numbers in parentheses refer to those in the main text.

Symbol	Definition
Design of experiments (Eq. 1)	
$\boldsymbol{D}$	Design matrix
n	Number of design points
$p_1,\ p_2,\ p_3$	Numbers of continuous, discrete numeric, and nominal factors
x_{il}, x_{jl}	lth continuous-factor values for design points i and j
u_{ik}, u_{jk}	kth discrete numeric factor values for design points i and j
v_{ih}, v_{jh}	Levels of the hth nominal factor for design points i and j
m_k	Number of levels of the kth discrete-numeric factor
L_h	Number of levels of the hth nominal factor
$I(\cdot)$	Indicator function (1 if the argument is true, 0 otherwise)
ψ	MaxPro design-quality criterion
Multi-output surrogate model — CoMOGP (Eqs. 2–6)	
$\mathbf{X}$	Input variable vector
$\mathbf{x}, \mathbf{x}^*$	Realisation of $\mathbf{X}$; new test input
$y_d(\mathbf{x})$	Response of the dth output at input $\mathbf{x}$
d, D	Output index and total number of outputs ($D = 24$ rib responses)
$g_q(\mathbf{x})$	qth shared latent function
$h_d(\mathbf{x})$	Output-specific latent function for output d
Q	Number of shared latent functions ($Q = 3$)
$a_{d,q}$	Mixing coefficient from shared latent q to output d
ϵ_d	Gaussian observation noise for output d
$\mathbf{u}_q$	Shared inducing variables for the qth shared latent function
$\mathbf{v}_d$	Individual inducing variables for the output-specific latent function of output d
$\mathbf{Z}_{\mathrm{q}}$	Inducing input locations for the qth shared latent function
$\mathbf{Z}_{\mathrm{d}}^{h}$	Inducing input locations for the dth output-specific latent function
M_g, M_h	Numbers of shared and output-specific inducing points ($M_g = 60, M_h = 30$)
$p(\mathbf{g} \mid \mathbf{u}), p(\boldsymbol{h} \mid \boldsymbol{v})$	Conditional GP priors of shared / output-specific latent function values
$q(\mathbf{u}, \mathbf{v})$	Variational posterior over the inducing variables
$k_{\mathrm{SE}}(\cdot,\cdot)$	Squared-exponential kernel with ARD (continuous inputs)
$k_{\mathrm{cat}}(\cdot,\cdot)$	Categorical kernel (posture)
$\mathbf{x}_i, \boldsymbol{x}_j$	Continuous input vectors of samples i and j
c_i, c_j	Posture levels of samples i and j
PDD-based sensitivity analysis (Eqs. 7–10)	
Y	Response variable
$f_{S,m}(\mathbf{X})$	Truncated PDD approximation of Y
N	Number of input variables ($N = 6$)
m	Polynomial order ($m = 3$)
S	Interaction dimension ($S = 2$)
f_0	Constant mean term
$\psi_{ij}(X_i)$	jth order orthonormal (Legendre) polynomial basis for input X_i
α_{ij}	Coefficient of the univariate term
$\beta_{i_1 i_2 j_1 j_2}$	Coefficient of the bivariate interaction term
V_i	Partial variance attributed to the main effect of X_i
V_{i_1,i_2}	Partial variance attributed to the interaction between X_{i_1} and X_{i_2}
$\mathrm{Var}[Y]$	Total variance of response Y
S_i	First-order sensitivity index of X_i
S_{i_1,i_2}	Second-order sensitivity index of the pair (X_{i_1}, X_{i_2})
T_i	Total-effect sensitivity index of X_i

Appendix B: Seat-belt hard-point modification configurations

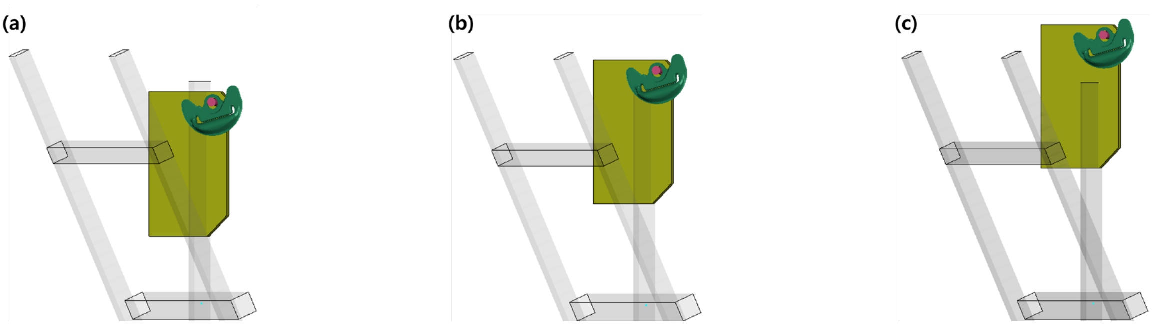

Fig. B1. D-ring Z-position configurations: (a) $X_1 = -50$ mm, (b) baseline position, and (c) $X_1 = 50$ mm.

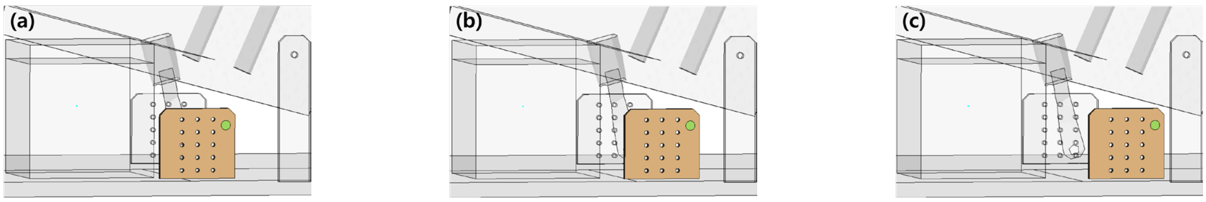

Fig. B2. Lap-belt anchor X-position configurations: (a) $X_2 = -30$ mm, (b) baseline position, and (c) $X_2 = 30$ mm.

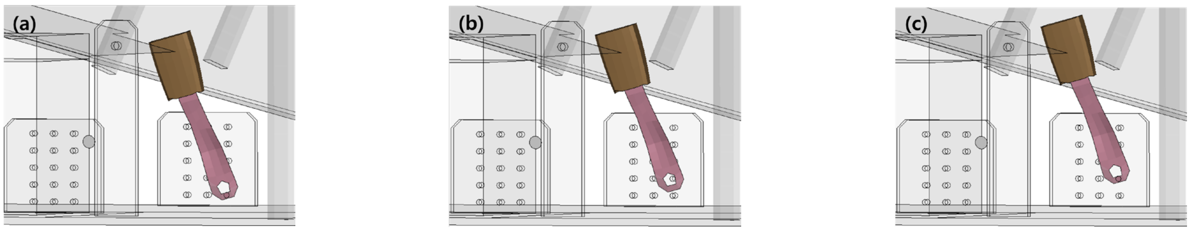

Fig. B3. Buckle Z-position configurations: (a) baseline position, (b) $X_3 = 10$ mm, and (c) $X_3 = 20$ mm.

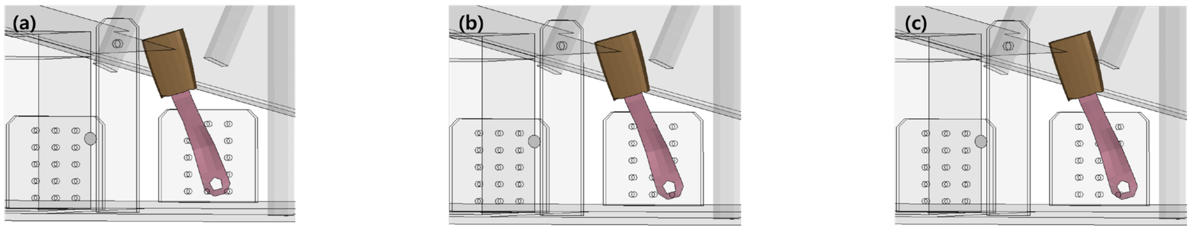

Fig. B4. Buckle X-position configurations: (a) $X_4 = -10$ mm, (b) baseline position, and (c) $X_4 = 10$ mm.

Appendix C: Sled pulse profiles for impact severity levels

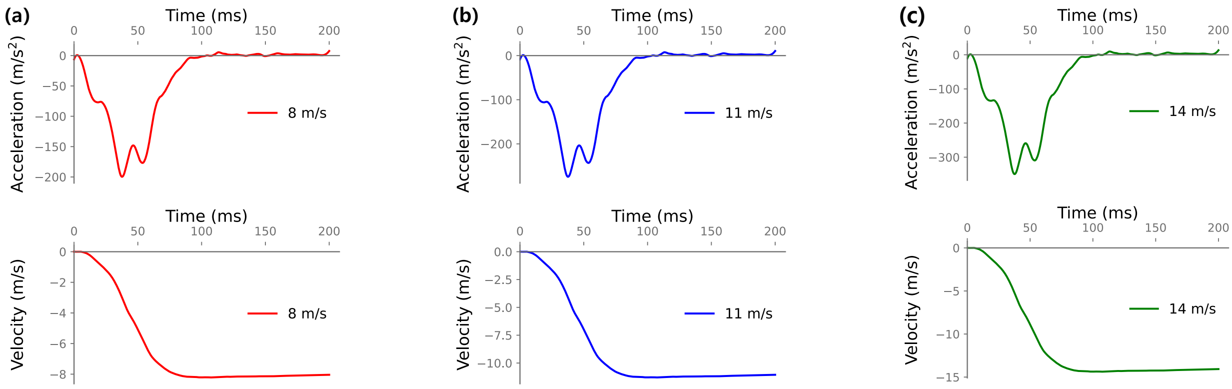

Fig. C1. Sled deceleration and velocity profiles used for the three impact severity levels: (a) ΔV = 8 m/s, (b) ΔV = 11 m/s, and (c) ΔV = 14 m/s.

Appendix D: PMHS and GHBMC model configuration in the baseline sled set-up

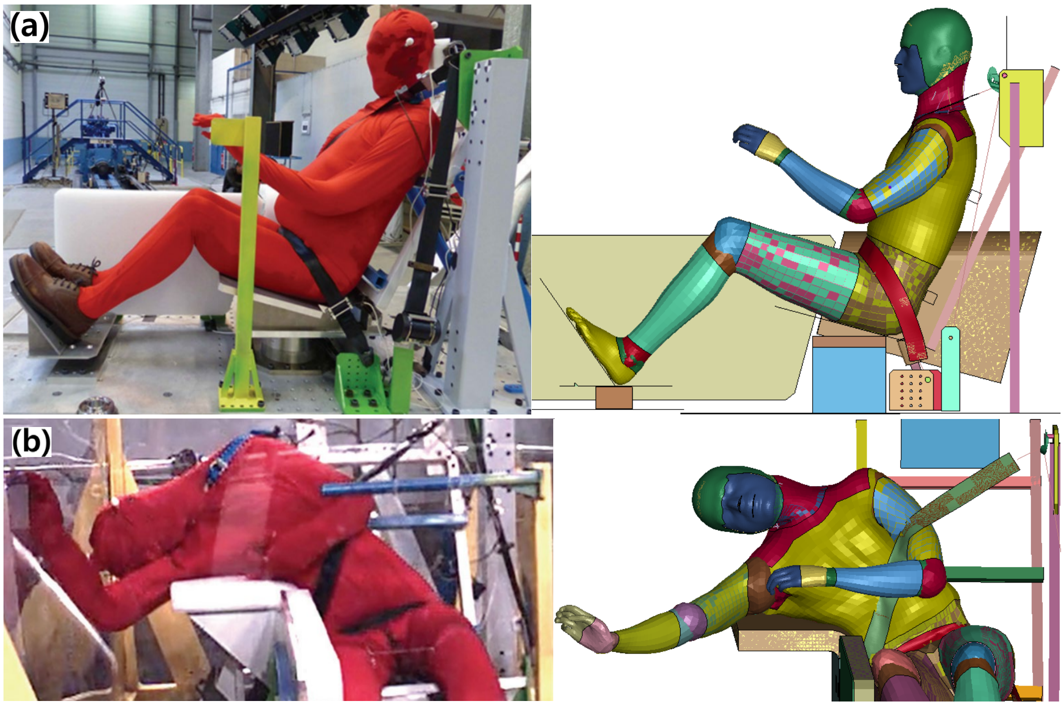

Fig. D1. Comparison of the PMHS and GHBMC model in the baseline sled set-up based on [2]: (a) side views of the PMHS and GHBMC model installed in the set-up; (b) comparison of PMHS and GHBMC model kinematics.

Appendix E: Baseline validation – head kinematics and contact forces

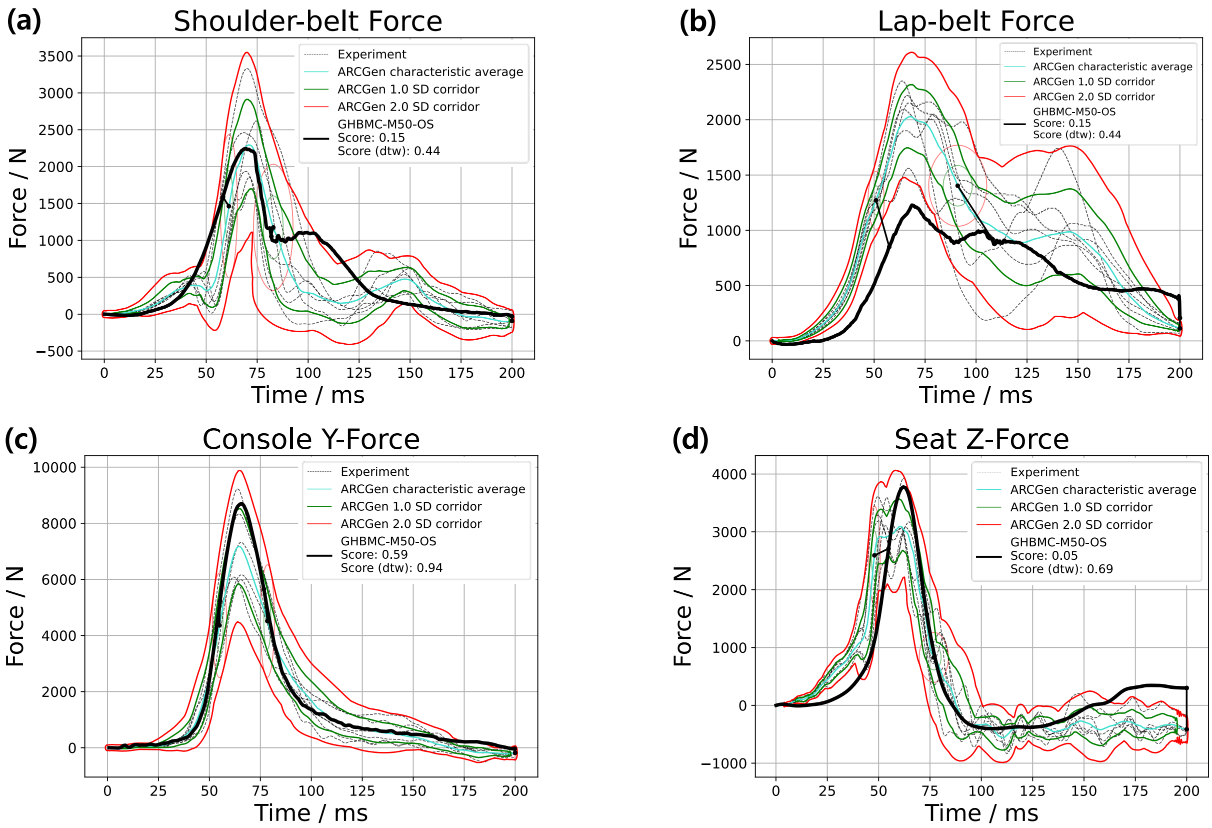

Fig. E1. Comparison of the baseline HBM responses with the PMHS corridors for qualitative validation force responses: (a) shoulder-belt force, (b) lap-belt force, (c) console Y-force, and (d) seat Z-force.

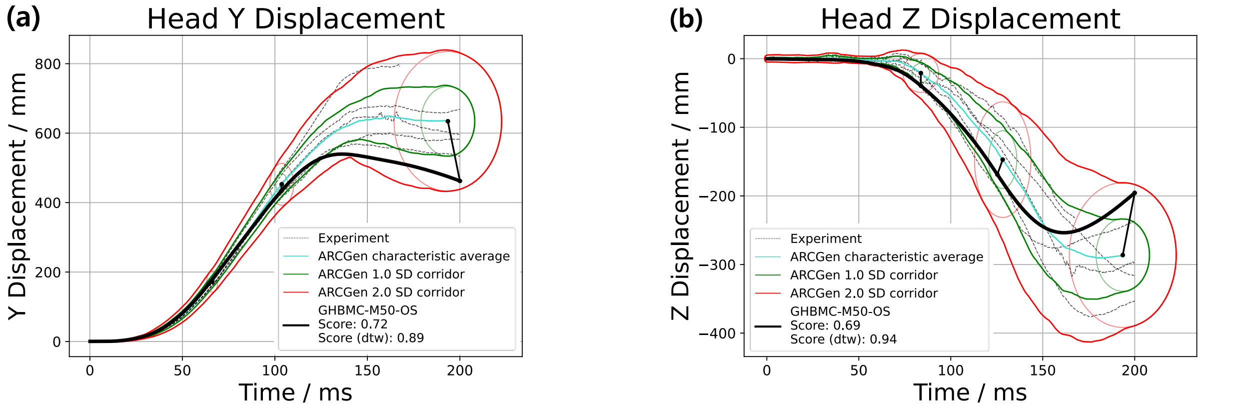

Fig. E2. Comparison of the baseline HBM responses with the PMHS corridors for (a) head Y displacement and (b) head Z displacement.

Appendix F: DOE optimisation results

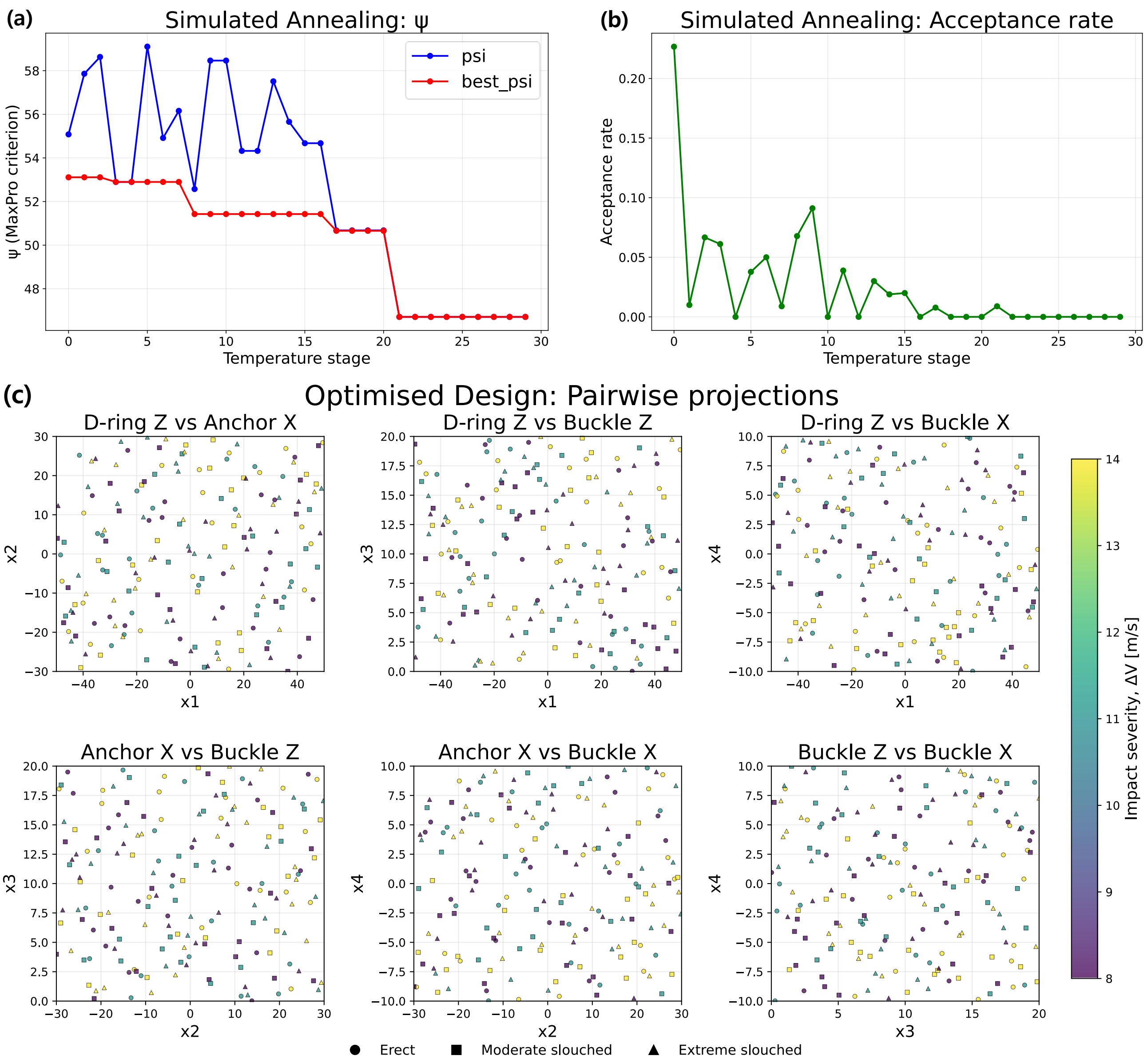

Fig. F1. DOE optimisation results: (a) evolution of the ψ criterion during optimisation, (b) simulated-annealing acceptance rate, and (c) pairwise projections of the final optimised DOE in the continuous design space.

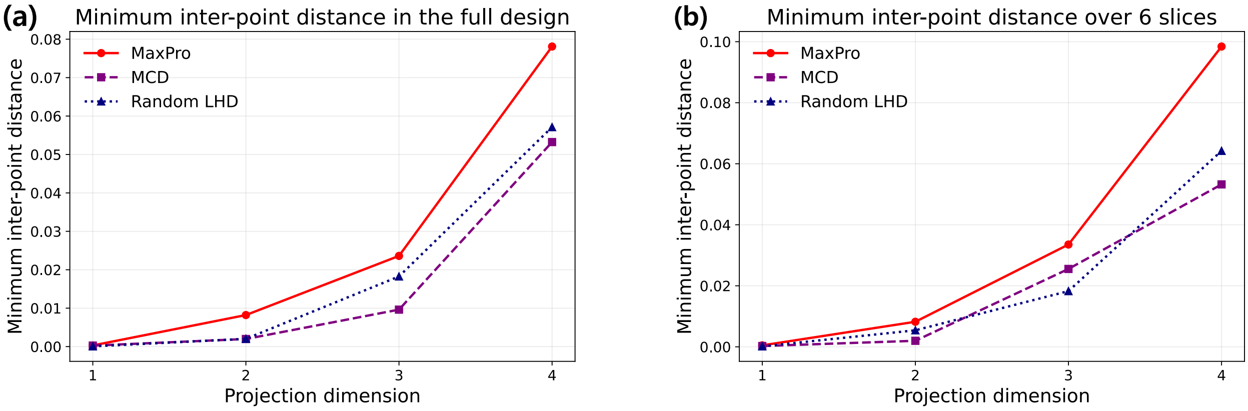

Fig. F2. Comparison of the minimum inter-point distances for the optimised MaxPro design, random LHD, and MCD across projection dimensions in (a) the full design space and (b) the six one-factor slices obtained by separately partitioning the continuous-variable design according to impact severity and occupant posture.

Appendix G: PDD-based global sensitivity results for all ribs

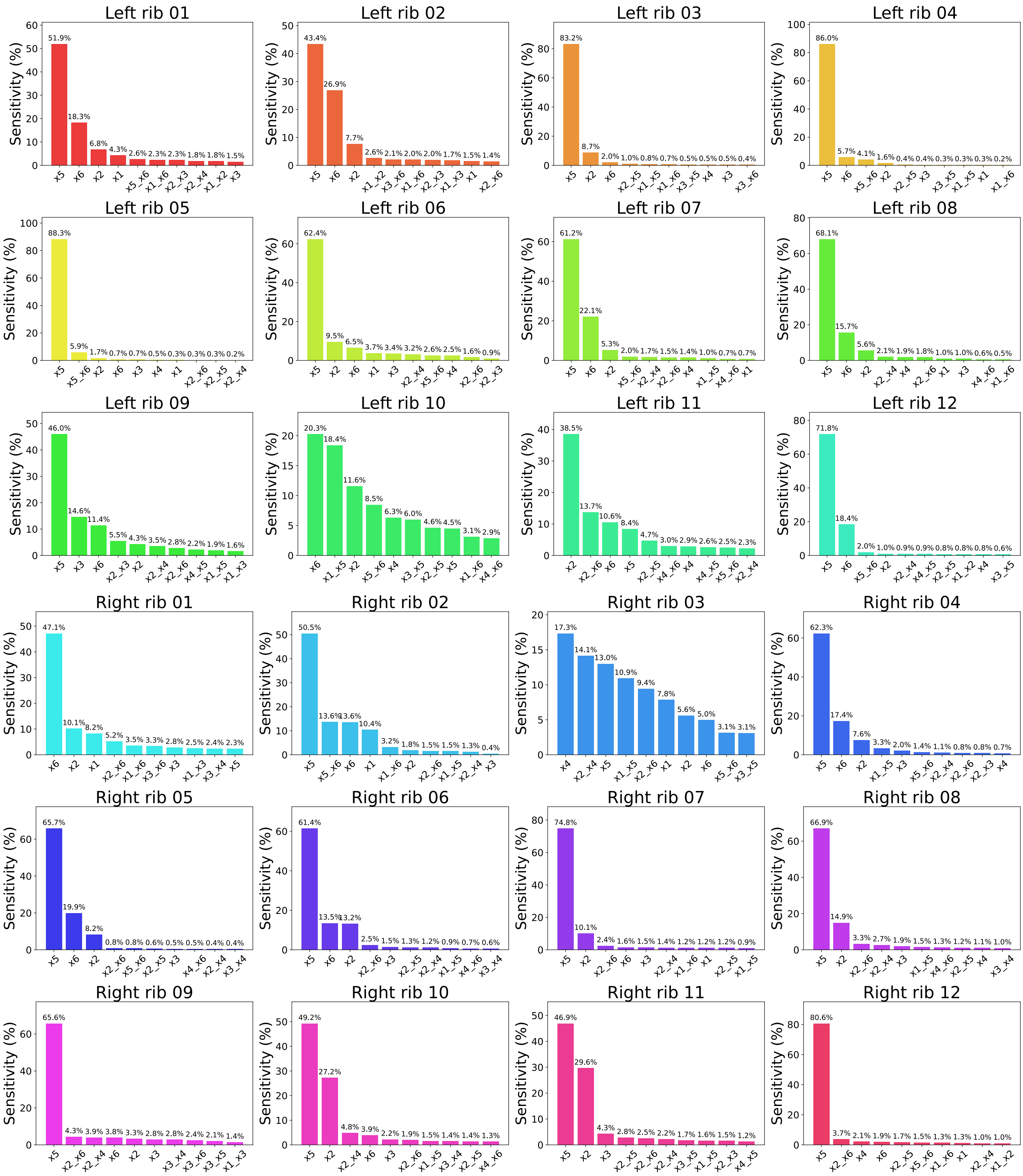

Fig. G1. PDD-based global sensitivity results for all left and right rib strain responses. Bars show the relative contributions of the dominant variables and interactions to the variance of each response. X_1: D-ring Z-position; X_2: lap-belt anchor X-position; X_3: buckle Z-position; X_4: buckle X-position; X_5: impact severity; X_6: occupant posture. Terms of the form X_i denote main effects, whereas terms of the form $X_i\_X_j$ denote pairwise interaction effects.

Appendix H: Full comparison of CoMOGP and SOGP predictive performance

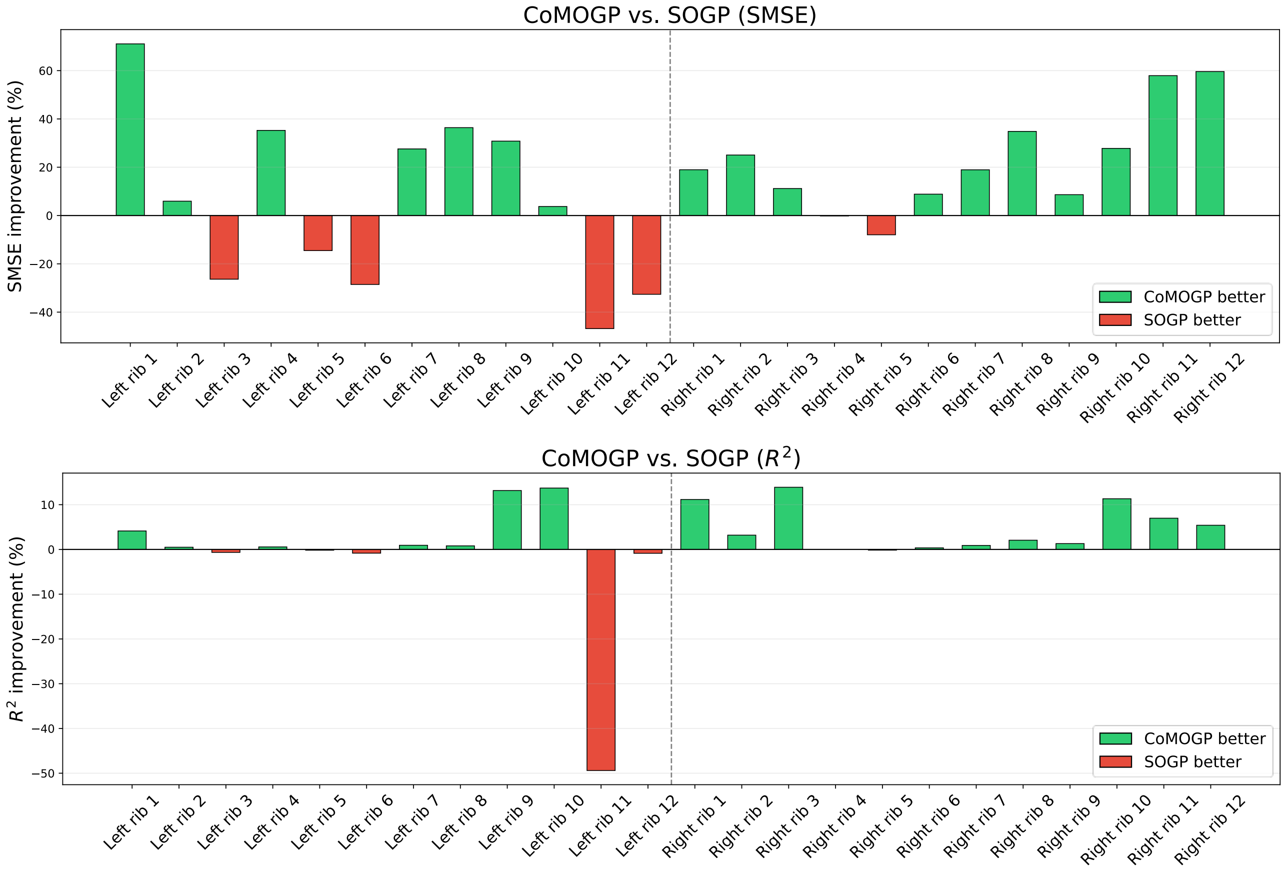

Fig. H1. Rib-wise comparison of predictive performance between SOGP and CoMOGP for the independent 27-case validation set, showing (top) SMSE and (bottom) R^2 for the left and right rib strain responses.

TABLE HI

COMPARISON OF COMOGP AND SOGP PREDICTIVE PERFORMANCE FOR ALL RIB STRAIN RESPONSES

Output	CoMOGP (SMSE)	SOGP (SMSE)	CoMOGP (R^2)	SOGP (R^2)
Left rib 1	0.015888	0.054948	0.984111	0.945049
Left rib 2	0.072342	0.076913	0.927599	0.923024
Left rib 3	0.030774	0.024354	0.969221	0.975642
Left rib 4	0.010156	0.015684	0.989843	0.984315
Left rib 5	0.013319	0.011632	0.986676	0.988364
Left rib 6	0.036407	0.028324	0.963501	0.971605
Left rib 7	0.023525	0.032488	0.976426	0.967444
Left rib 8	0.013734	0.021592	0.986252	0.978387
Left rib 9	0.206497	0.298431	0.792861	0.700642
Left rib 10	0.737202	0.765852	0.243702	0.21431
Left rib 11	0.748553	0.509857	0.246211	0.486576
Left rib 12	0.034189	0.02578	0.965797	0.97421
Right rib 1	0.268848	0.331761	0.699786	0.629533
Right rib 2	0.084559	0.112827	0.915273	0.886949
Right rib 3	0.484141	0.545099	0.507878	0.445915
Right rib 4	0.023285	0.023246	0.976694	0.976733
Right rib 5	0.020593	0.019073	0.979375	0.980897
Right rib 6	0.035289	0.038715	0.964552	0.96111
Right rib 7	0.036302	0.044784	0.963608	0.955105
Right rib 8	0.036222	0.055579	0.963575	0.94411
Right rib 9	0.120056	0.13141	0.879944	0.868589
Right rib 10	0.205476	0.2846	0.791012	0.710535
Right rib 11	0.04488	0.106669	0.954752	0.892455
Right rib 12	0.033557	0.08311	0.966443	0.916889
Overall	0.138991	0.15178	0.858129	0.844933